Electronic Supplementary Material (ESI) for Chemical Science.
This journal is © The Royal Society of Chemistry 2021

Electronic Supplementary Information (ESI)

Non-concentrated aqueous electrolytes with organic solvent additives for stable zinc batteries

Yang Dong,§[a] Licheng Miao,§[bc] Guoqiang Ma,[a] Shengli Di,[a] Yuanyuan Wang,[a] Liubin Wang,[ab] Jianzhong Xu[a] and Ning Zhang*[ab]

[a] College of Chemistry & Environmental Science, Key Laboratory of Analytical Science and Technology of Hebei Province, Hebei University, Baoding 071002, China. E-mail: ningzhang@hbu.edu.cn

[b] Key Laboratory of Advanced Energy Materials Chemistry (Ministry of Education), College of Chemistry, Nankai University, Tianjin 300071, China.

[c] College of Physics and Optoelectronic Engineering, Shenzhen University, Shenzhen 518060, China.

§ These authors contributed equally to this work.

Experimental Section

Materials. The $Zn(OTf)_2$-based aqueous electrolytes with different amount of DMC additives were prepared by dissolving the desired amount of salts into the selected solvents. The molar ratios between water and DMC solvents range from 8:1, 6:1, 4:1, to 2:1, and the corresponding electrolytes are denoted as W8D1, W6D1, W4D1, and W2D1, respectively. The neat 2 m $Zn(OTf)_2$ aqueous electrolyte without adding DMC is denoted as 2 m W. Taking the W4D1 electrolyte as an example, H_2O and DMC solvents with a molar ratio of 4:1 were mixed firstly, and then 2 m $Zn(OTf)_2$ was dissolved into the bi-solvent system. V_2O_5 active materials were prepared by simply ball-milling the commercial V_2O_5 with graphite powders (mass ratio = 8:2) at a speed of 400 rpm for 4 h. The layered δ-MnO_2 was synthesized by a hydrothermal method.[1] Typically, $KMnO_4$ and $MnSO_4$ with a molar ratio of 6:1 were dissolved into deionized water, and the mixed solution was loaded into a 100 mL Teflon-lined autoclave and maintained at 160 ^oC for 12 h. The obtained MnO_2 powders were centrifuged, washed thoroughly using water, and dried at 80 ^oC for 10 h. The ZnHCF was synthesized using a co-precipitation method. Typically, 30 mL of 0.1 M $ZnSO_4$ and 30 mL of 0.05 M $K_3Fe(CN)_6$ solutions were simultaneously added into 30 mL deionized water under stirring at 60 ^oC for 6 h. The obtained product was centrifuged, washed using water, and then dried at 70 ^oC for 10 h.

Characterization. Raman spectra of the H_2O+DMC electrolyte systems were performed on a Horiba HR-Evolution Raman microscope using 532 nm excitation. For the Raman test, the electrolyte samples were sealed in capillary tubes. XRD patterns were characterized on a Bruker D8 ADVANCE (Cu Kα radiation) at a scanning rate of 4^o min^{-1}. SEM images were obtained on a field-emission scanning electron microscope (JEOL JSM-7500F). XPS spectra were conducted on a ESCALAB 250Xi spectrometer (ThermoFisher). All of the binding energies were referenced to the C 1s peak (284.8 eV). The ^{17}O NMR experiments were obtained on a Bruker Avance III spectrometer. Contact angle tests were measured on Dataphysics OCA15 optical contact angle system.

Electrochemical tests. The reversibility of Zn plating/stripping in H_2O+DMC electrolytes were measured using Zn/Ti cells with a cut-off charging potential of 0.5 V.[2] Symmetric Zn/Zn cells were employed to study the reversibility and stability of H_2O+DMC electrolytes. LSV was performed in a three-electrode configuration using Ti foil as a working electrode and Zn foils as the reference and counter electrodes. Electrochemical performances of Zn-ion full batteries were evaluated using CR2032 coin-type cells with V_2O_5 (δ-MnO_2 or ZnHCF) cathode, glass fiber separator, and Zn foil anode. The working electrode was fabricated by blending active materials powder, Super P carbon, and polyvinylidene fluoride in a weight ratio of 8:1:1 using N-methyl-2-pyrrolidone as solvent. The slurry mixture was pasted onto Ti foil or stainless steel mesh, and dried at 80 ^oC for 10 h under vacuum. The as-prepared electrodes were cut into round slices with a typical mass loading of ~2 mg cm^{-2}. EIS, ionic conductivity tests, and CV profiles were performed on a CHI660E

electrochemical work station. Charge/discharge of battery was tested on an LAND-CT2001A battery-testing instrument. Calculation of specific capacity and current density was based on the active cathode mass.

Computational details

Molecular Dynamics Simulations. Molecular dynamics (MD) simulations were conducted on the $Zn(OTf)_2$-(DMC)-H_2O solutions for exploring changes in the zinc solvation shell as a function of DMC concentration. We simulated 6 different solution systems, denoted in the following as systems DMC-H_2O, 2 m W, W8D1, W6D1, W4D1, and W2D1 with the particular number of ions and molecules in the simulation box summarized in Table S2. MD simulations used the GROMACS 2018.4 simulation package[3] with the AMBER[4] force fields. The equilibrium and production simulations were all performed in the *Npt* ensemble at constant pressure (1.01325 bar) and temperature (298.15 K) in a cubic box with periodic boundary conditions in all *xyz* Cartesian directions. For equilibrium processes, the temperature is maintained by V-rescale coupling with a time constant of 0.2 ps. The Berendsen barostat was adopted for controlling pressure, which is with a coupling constant of 0.5 ps. Equilibrium simulation ran 10 ns (2fs per step, simulating $5*10^6$ steps). For production simulations, the V-rescale coupling and parrinello-rahman barostat were used to control the temperature and the pressure, respectively. Production simulation ran 100 ns (2fs per step, simulating $5*10^7$ steps) for obtaining the equilibrium Zn^{2+} coordination shell structure at room temperature for different concentrations of electrolytes. Electrostatic interactions were treated using the Particle-Mesh-Ewald (PME) method[5]. The coordination number of molecules of type *i* in the first solvation shell surrounding a single molecule of type *j* is calculated as:

$$N_i = 4\pi n_j \int_0^{R_M} g_{ij}(r) r^2 dr$$

in which R_M is the distance of the first minimum following the first peak in the radial distribution function (RDF), $g_{ij}(r)$, which is a standard approach for bulk liquid[6]. All the visualizations of MD simulations were implemented by VMD software.[7]

The ionic diffusion behavior is calculated by a time-dependent MSD (the Mean Square Displacement) which is defined by the reaction of $MSD(t) = \langle |r_i(t)-r_i(0)|^2 \rangle$, where $r_i(t)$ is the site of the *i*-th ions at the time *t*. Based on the Einstein equation, the diffusion coefficient *D* is given by the slope of MSD:

$$D = \lim_{t\to\infty} \frac{1}{6t} < r^2(t) >$$

Molar conductivity is obtained from the Nernst-Einstein equation:[8-10]

$$\Lambda = \frac{N_A e^2}{k_B T}(4D^{2+} + D^{-})$$

in which N_A is Avogadro's number, *e* is the electron charge, k_B is Boltzmann's constant, and *T* is the temperature (T=298.15 K).

Ionic conductivity (κ) is defined as:

$\kappa = \Lambda \times c$, where c is the molarity.

Density Functional Theory calculations. All calculations were performed using the Gaussian 16 package.[11] The structures of molecules and solvation sheaths were optimized at the B3LYP/6-311G(d) level for C, H, O, F, and S elements and B3LYP/SDD level for Zn. Frequency calculations were performed at the same level to confirm the obtained optimized stationary point. To investigate the influence of solvent, SMD solvation model[12] was employed with a dielectric constant of water. Calculations of Mulliken charge distribution is performed by GaussView.

Binding energy (E_b) between two components is defined as:

$E_b = E_{1,2} - E_1 - E_2 + E_{BSSE}$

in which $E_{1,2}$, E_1, and E_2 were the total energy of the 1 and 2 complexes, component 1, and component 2, respectively. E_{BSSE} is the BSSE (basis set superposition error) correction energy, which was applied to calculate the intermolecular interactions accurately.

The reduction potentials were calculated for the abovementioned 6 complexes surrounded by implicit solvent. The reduction potential of complex A was calculated as the negative of the free energy of formation of A^- in solution [$\Delta G^S_{298} = G^S_{298}(A^-) - G^S_{298}(A)$] divided by Faraday's constant as given by:

$$E_{red} = -\frac{\Delta G^S_{298K}}{F} - 3.656\text{V}$$

The difference between the Zn^{2+}/Zn scale and absolute reduction potential of 3.656 V was subtracted to convert DFT results to the Zn^{2+}/Zn scale as discussed extensively elsewhere. All the visualizations of DFT simulations were implemented by GaussView software.

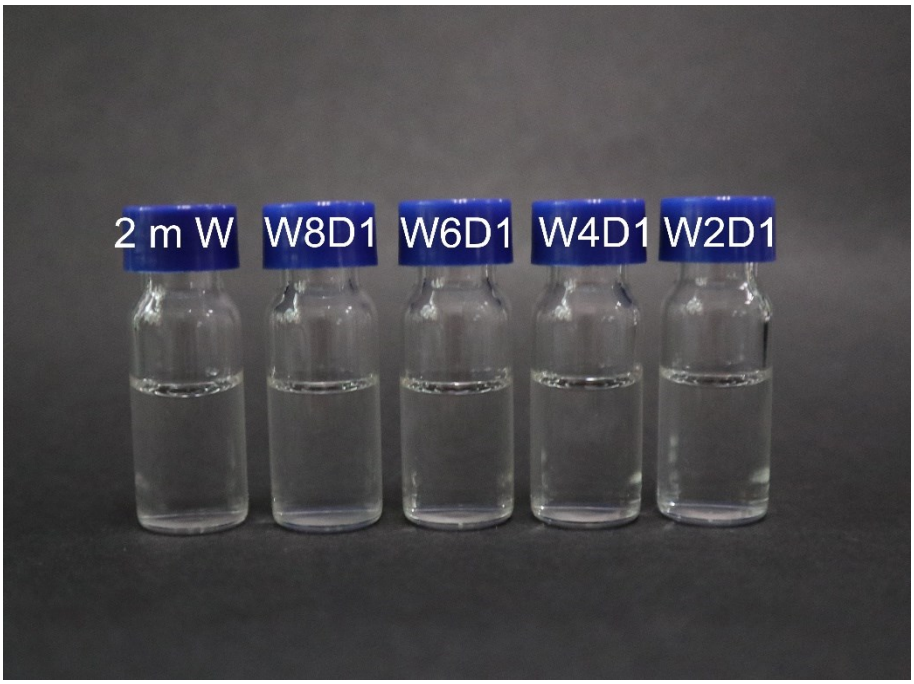

Fig. S1 Photographs of the 2 m W electrolyte and the homogeneous W8D1, W6D1, W4D1, and W2D1 electrolytes.

Fig. S2 Photograph of 0.1 m $Zn(OTf)_2$ in the neat DMC electrolyte. DMC solvent has a low solubility for $Zn(OTf)_2$ salt (< 0.1 m).

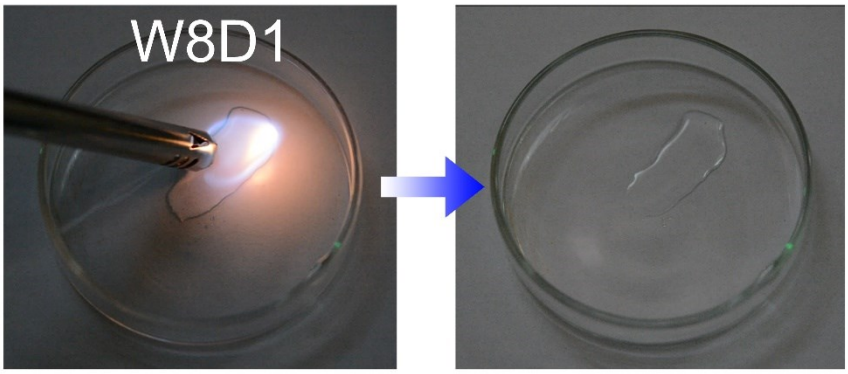

Fig. S3 Photographs of the ignition test of the W8D1 electrolyte.

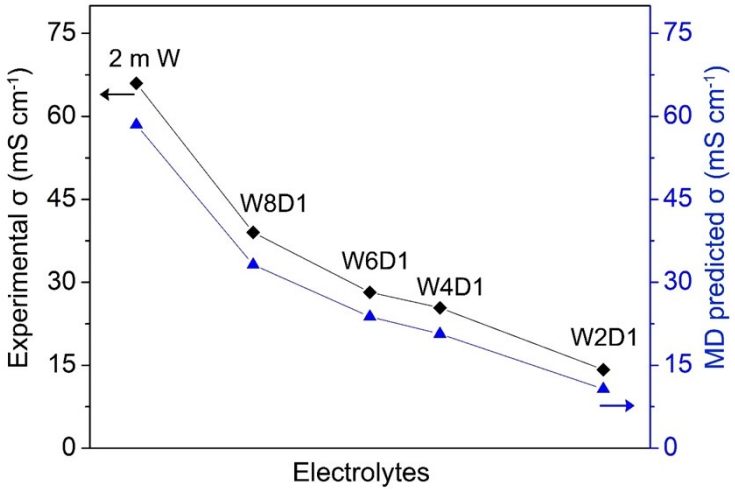

Fig. S4 Ionic conductivities (σ) of 2 m W, W8D1, W6D1, W4D1, and W2D1 electrolytes tested at room temperature along with the predicted conductivities by MD simulations.

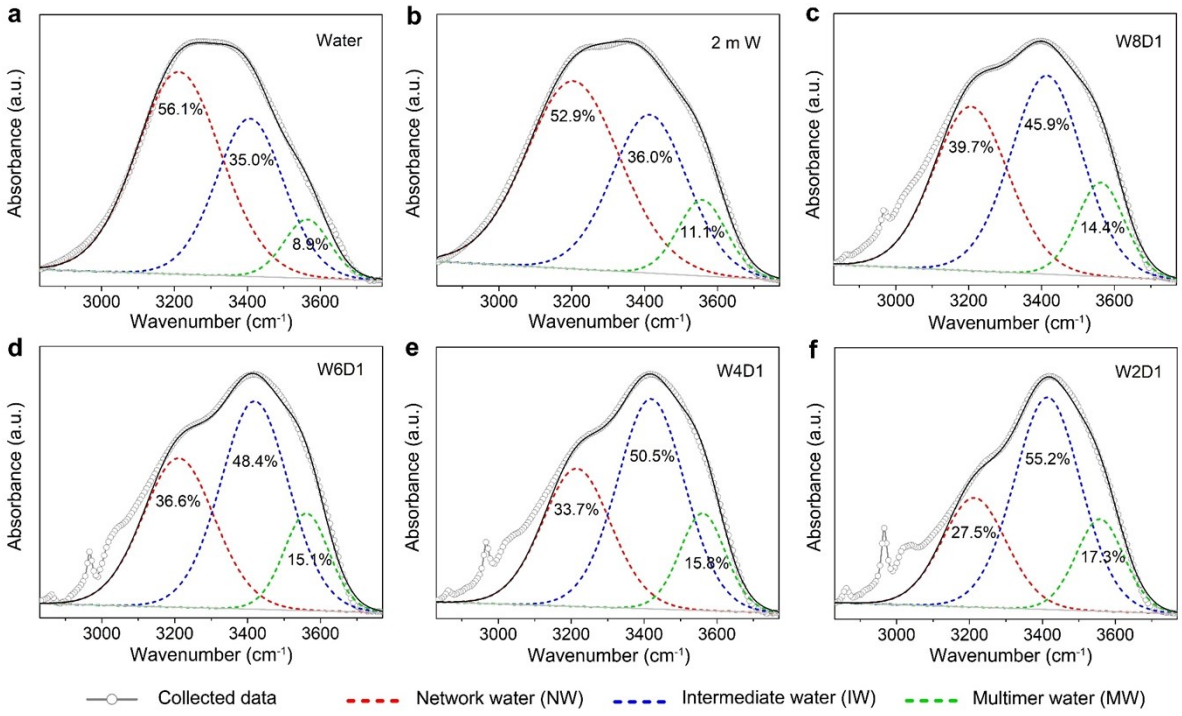

Fig. S5 FTIR spectra and corresponding fitted curves of different electrolytes: (a) water, (b) 2 m W, (c) W8D1, (d) W6D1, (e) W4D1, and (f) W2D1. Peaks within the range of 2800-3000 cm^{-1} shown in (c-f) can be assigned to C-H symmetric and asymmetric stretching of DMC.[13]

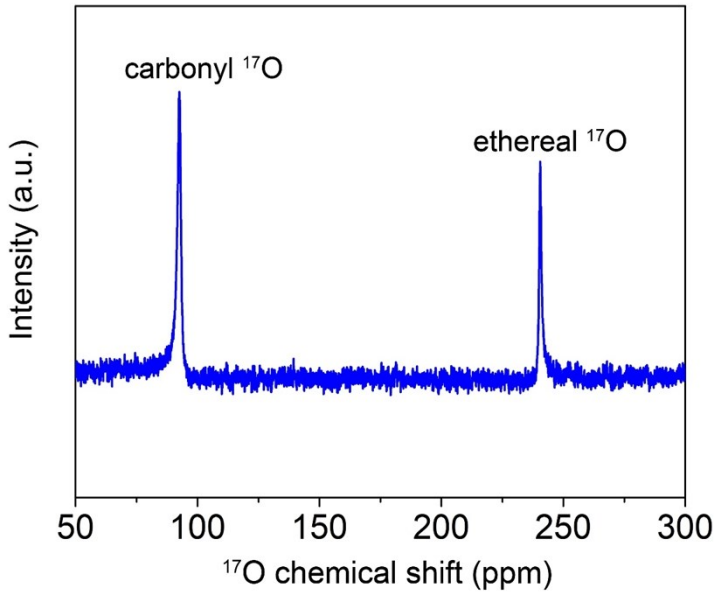

Fig. S6 ^{17}O NMR spectrum for the neat DMC solvent. Two ^{17}O signals located at around 93 and 240 ppm are attributed to the carbonyl ^{17}O and ethereal ^{17}O signals, respectively.[14]

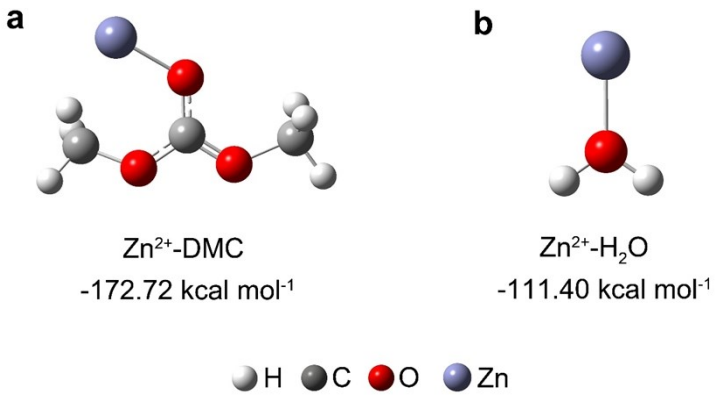

Fig. S7 Binding energy of (a) Zn^{2+}-DMC and (b) Zn^{2+}-H_2O complexes. A relatively lower binding energy indicates a stronger interaction between structures.[15]

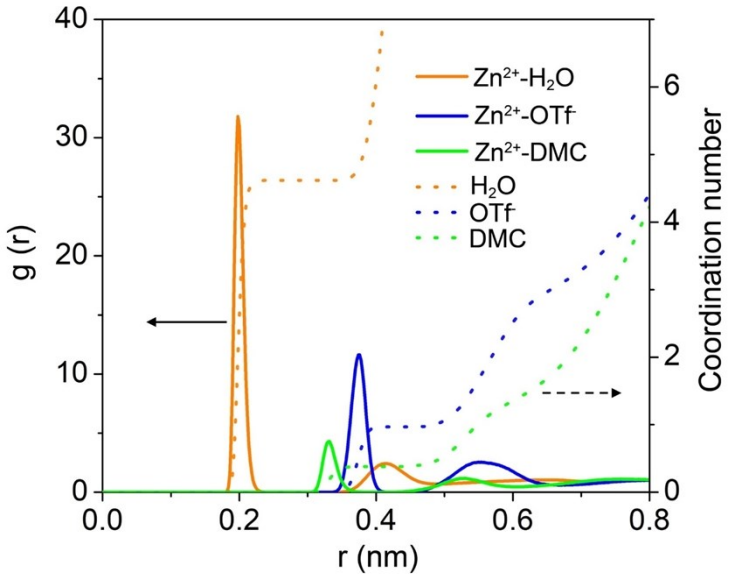

Fig. S8 RDFs of Zn-H_2O, Zn-DMC and Zn-OTf^- pairs, and the coordination numbers in W8D1 electrolyte. RDFs reveal that the Zn^{2+}-solvation sheath in W8D1 is occupied primarily by 4.6 H_2O molecules, 0.4 DMC solvent, and 1.0 OTf^- anion on average (i.e., $Zn^{2+}[H_2O]_{4.6}[DMC]_{0.4}[OTf^-]_{1.0}$).

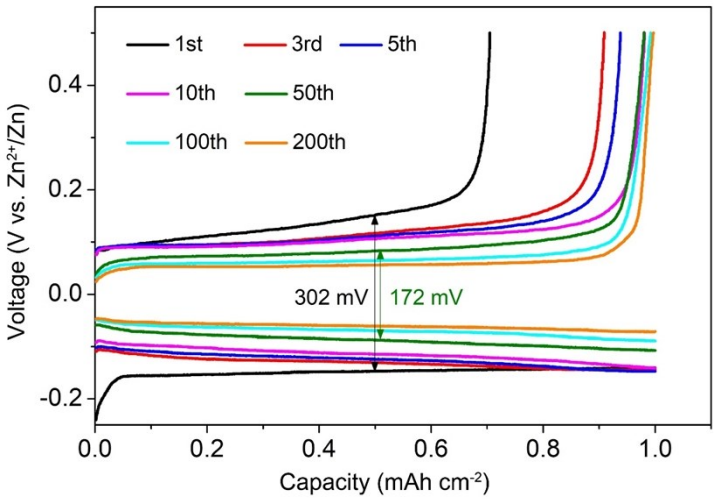

Fig. S9 Typical voltage profiles of Zn/Ti cell in W2D1 electrolyte at 1 mA cm^{-2} with a plating capacity of 1 mAh cm^{-2}.

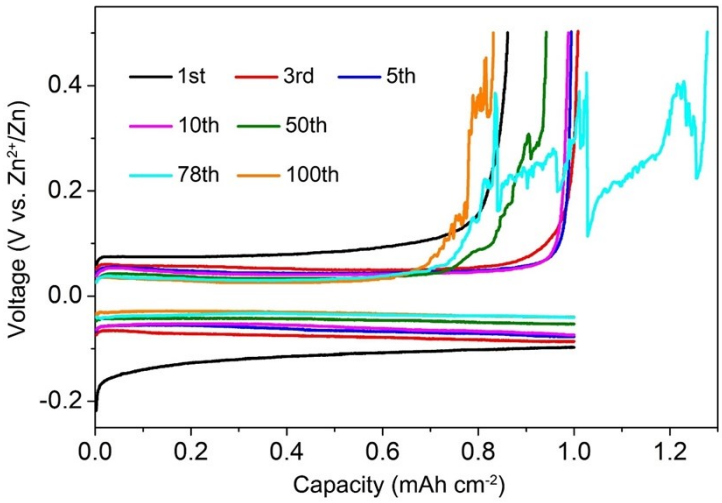

Fig. S10 Typical voltage profiles of Zn/Ti cell in W8D1 electrolyte at 1 mA cm^{-2} with a plating capacity of 1 mAh cm^{-2}.

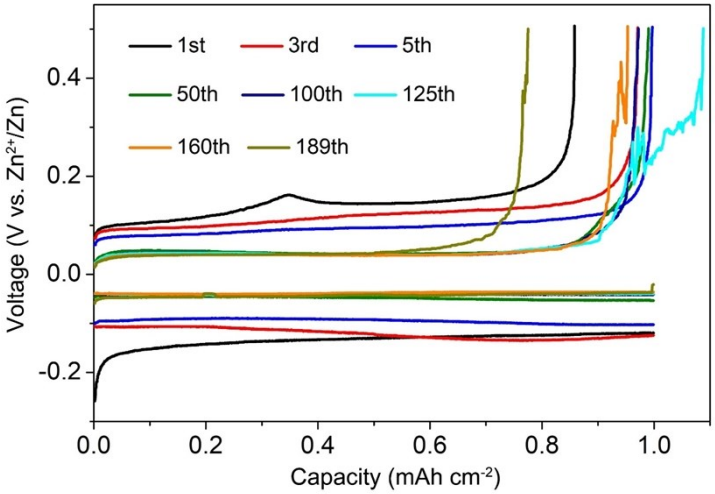

Fig. S11 Typical voltage profiles of Zn/Ti cell in W6D1 electrolyte at 1 mA cm^{-2} with a plating capacity of 1 mAh cm^{-2}.

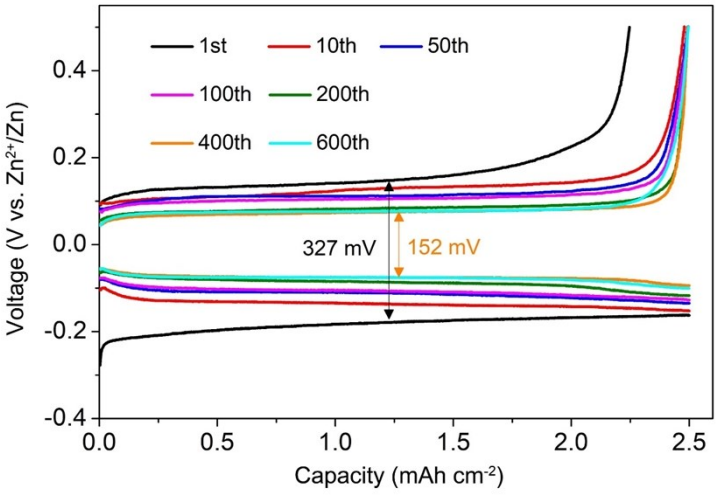

Fig. S12 Selected voltage profiles of Zn/Ti cell in W4D1 electrolyte at 5 mA cm^{-2} with a deposition capacity of 2.5 mAh cm^{-2}.

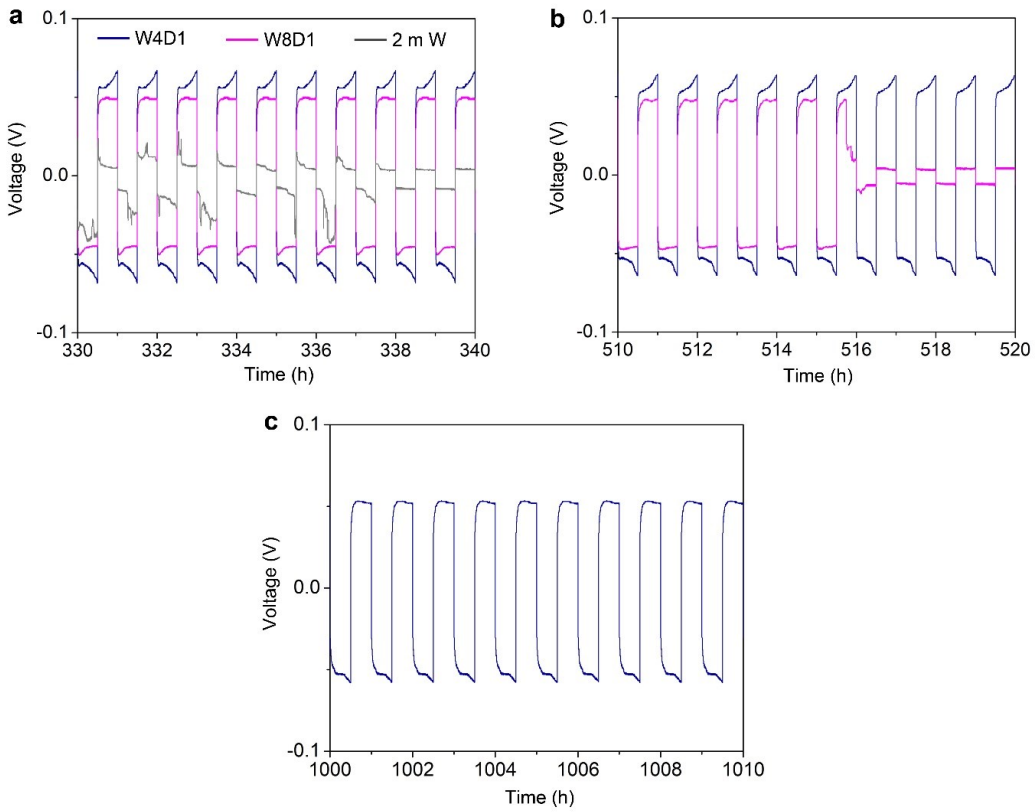

Fig. S13 Typical voltage profiles of Zn/Zn cells in W4D1, W8D1 and 2 m W electrolytes at 1 mA cm^{-2} during different test time of (a) 330-340 h, (b) 510-520 h, and (c) 1000-1010 h. After 1000 cycles, the Zn electrode in W4D1 exhibits a rectangular shape of Zn^{2+} plating/stripping with a smaller polarization, which may due to the enhanced hydrophilicity[16,17] of the cycled Zn with a smaller contact angle of electrolyte (Fig. S19) than that of the pristine Zn electrode (Fig. S18).

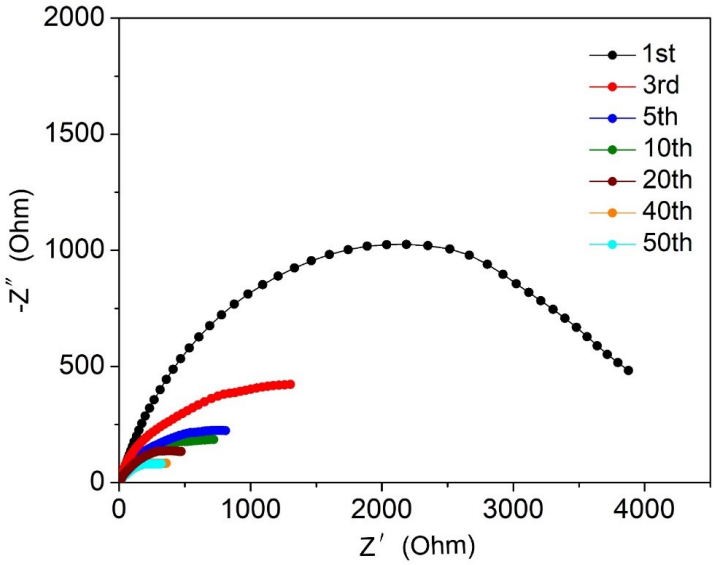

Fig. S14 EIS spectra of Zn/Zn cells in W4D1 electrolyte at selected cycles.

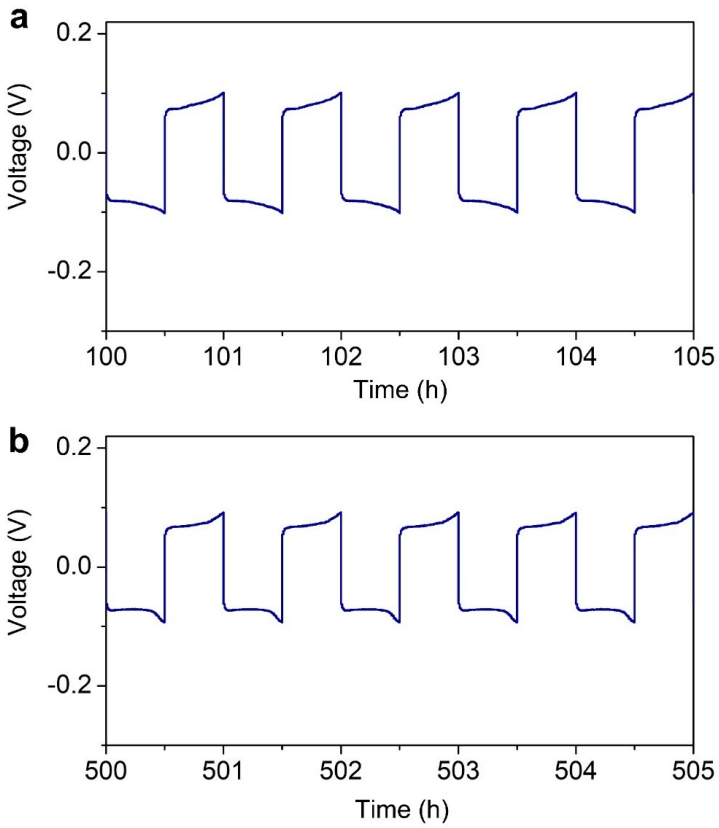

Fig. S15 Typical voltage profiles of Zn/Zn cells in W4D1 electrolyte at 5 mA cm^{-2} during the test time of (a) 100-105 h and (b) 500-505 h.

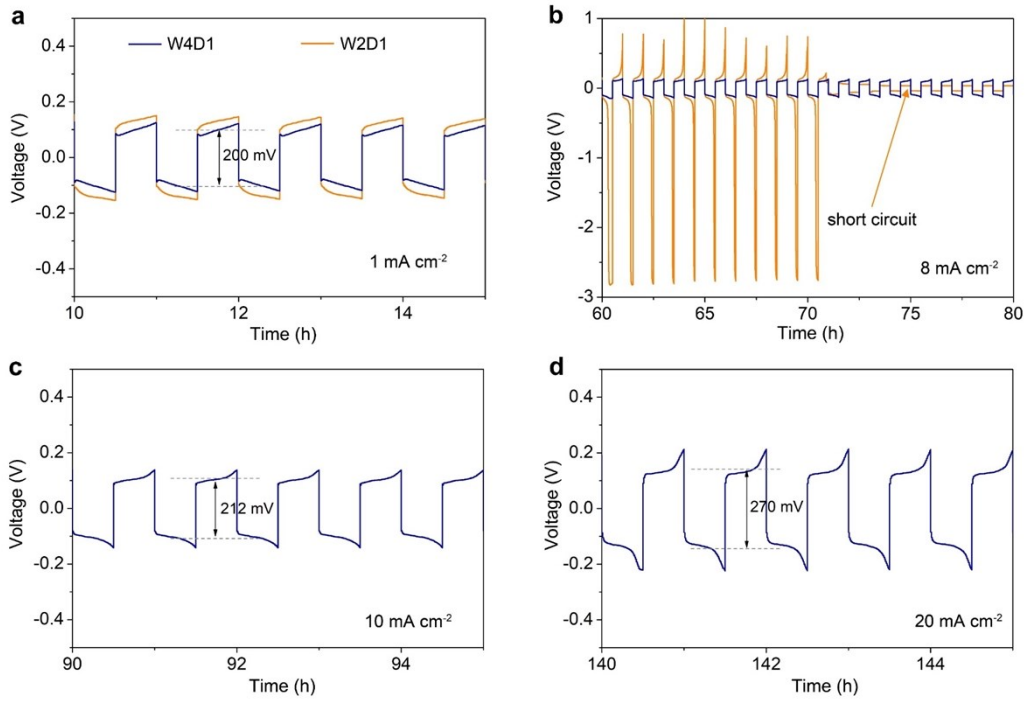

Fig. S16 Typical voltage profiles of Zn/Zn cells in W4D1 and W2D1 electrolytes at (a) 1, (b) 8, (c) 10, and (d) 20 mA cm^{-2}.

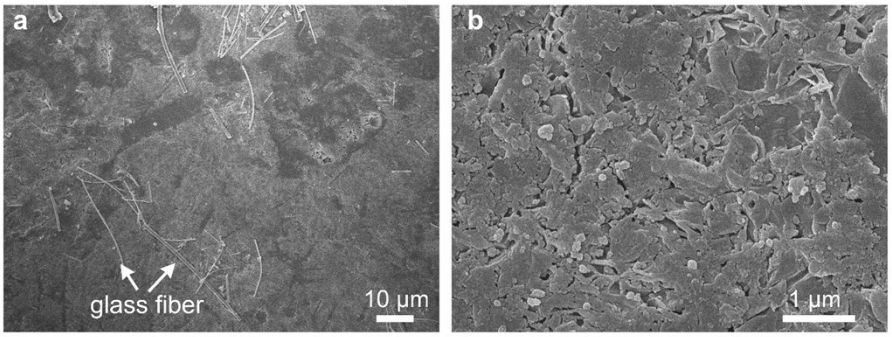

Fig. S17 (a) Low-magnification and (b) high-magnification SEM images of the Zn electrode after 1050 cycles in W4D1 at 1 mA cm^{-2}.

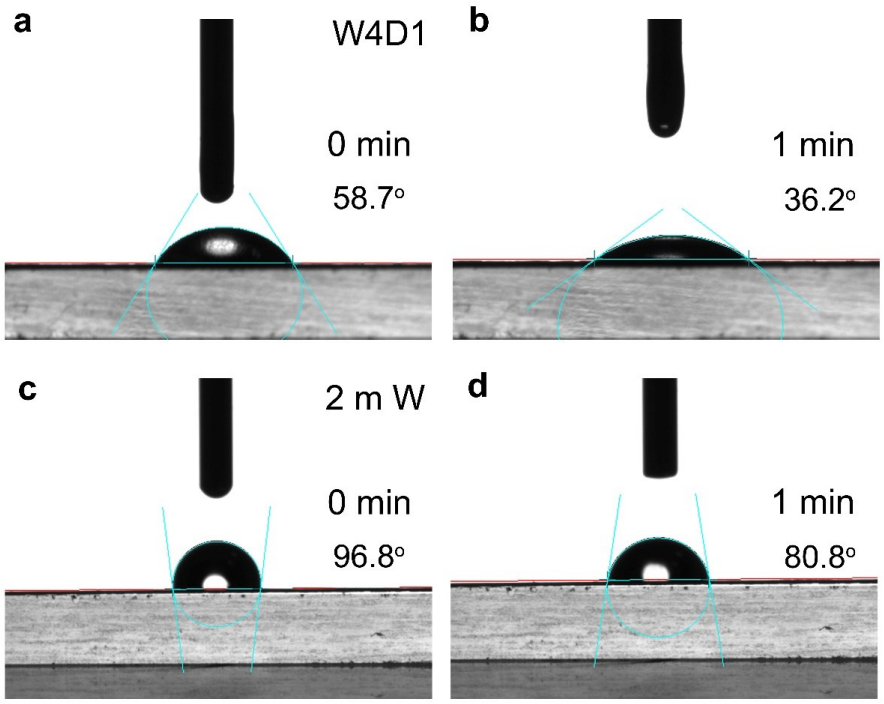

Fig. S18 Contact angles of (a,b) W4D1 electrolyte and (c,d) 2 m W electrolyte on the pristine Zn foil during different periods.

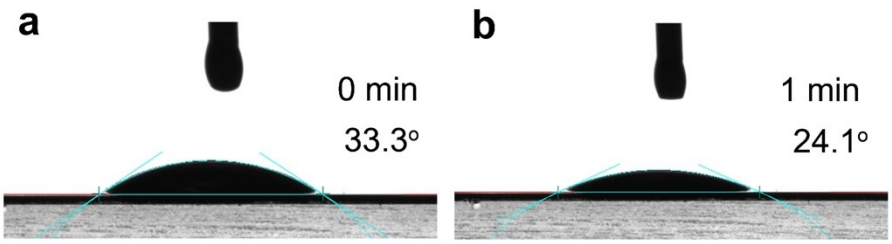

Fig. S19 Contact angles of W4D1 electrolyte on the cycled Zn electrode (re-obtained from Zn/Zn cell after 1050 cycles at 1.0 mA cm^{-2}) at (a) the initial state and (b) the state after 1 min.

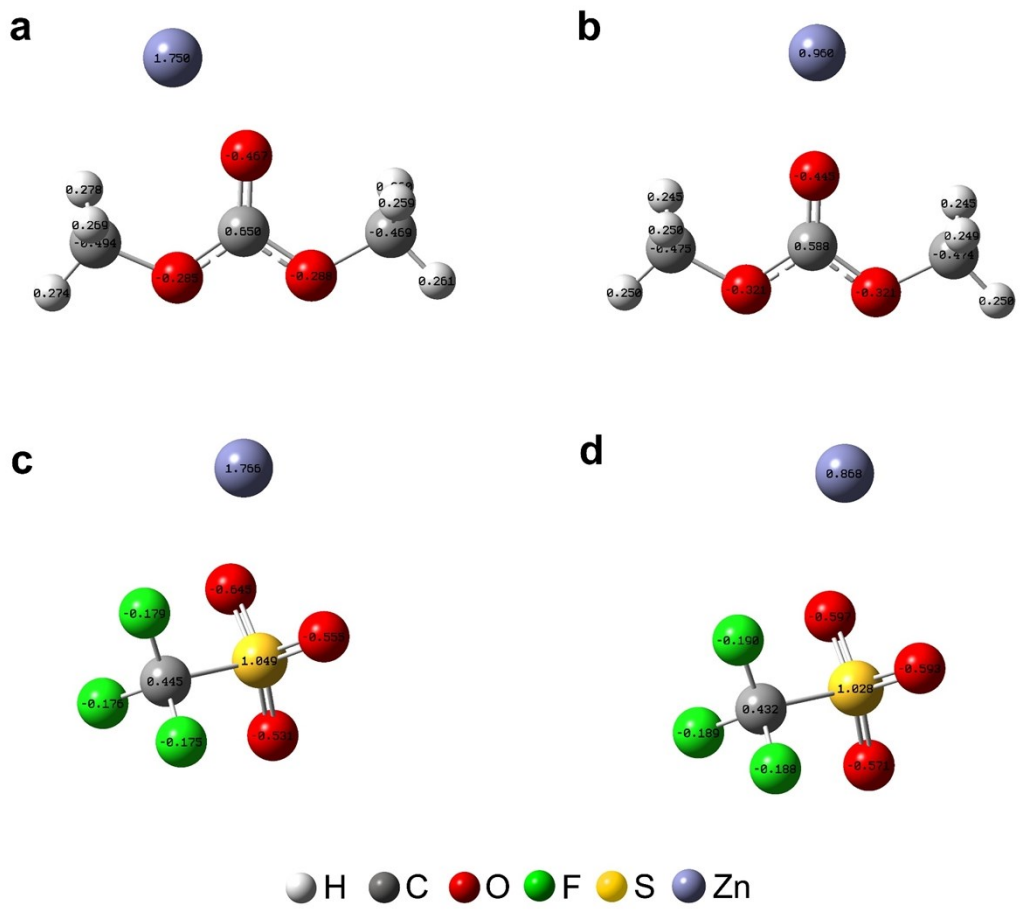

Fig. S20 Change in the atomic charges (predicted by the Mulliken analysis) for the (a,b) Zn^{2+}-DMC and (c,d) Zn^{2+}-OTf^- complexes (a,c) before and (b,d) after reduction. Previous works[18-21] have demonstrated that the electron could preferably transfer from cation to solvent (or anion) in the cation-solvent (or cation-anion) unit and induce the solvent/anion decomposition, which is a well-known electrolyte decomposition process, where the solid electrolyte interphase could be formed at the electrode interface.

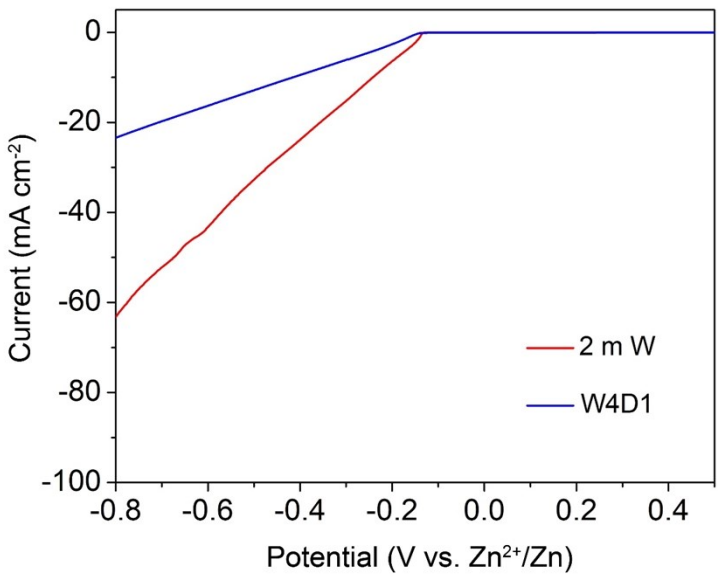

Fig. S21 LSV response curves for 2 m W and W4D1 electrolytes at 5 mV s^{-1}. The onset potentials of Zn^{2+} plating in W4D1 and 2 m W electrolytes are around -138.5 and -130.3 mV, respectively. Compared with 2 m W, the W4D1 electrolyte significantly suppresses the H_2 evolution as supported by a much reduced current response below -0.2 V (vs. Zn^{2+}/Zn).

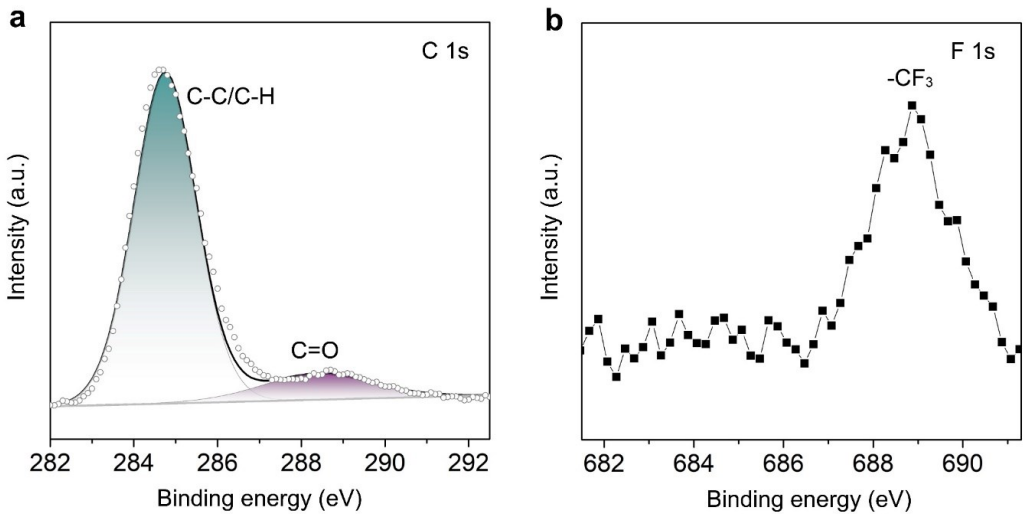

Fig. S22 XPS spectral regions for (a) C 1s and (b) F 1s on the Zn electrode in 2 m W electrolyte after 5 cycles. The C signal mainly comes from the adventitious carbon adsorbed on the substrate surface.[22] The $-CF_3$ species comes from either the trace salt or the incomplete reduction product of $Zn(OTf)_2$ on the Zn surface.

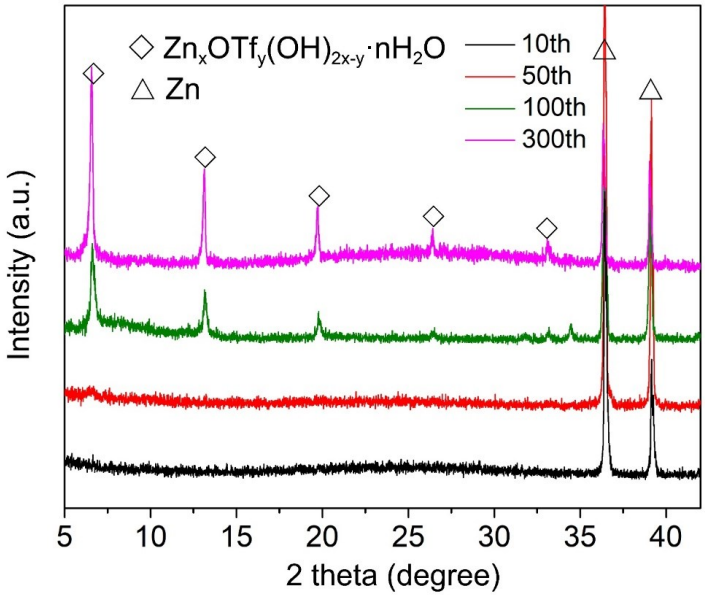

Fig. S23 XRD patterns of Zn electrodes (re-obtained from Zn/Zn cells) after 10, 50, 100 and 300 cycles in 2 m W electrolyte.

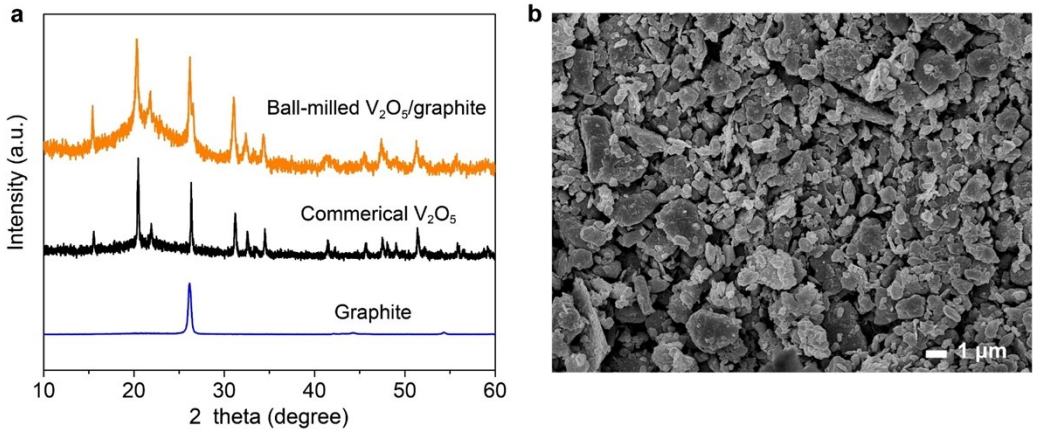

Fig. S24 (a) XRD pattern and (b) SEM image of the ball-milled V_2O_5/graphite composite.

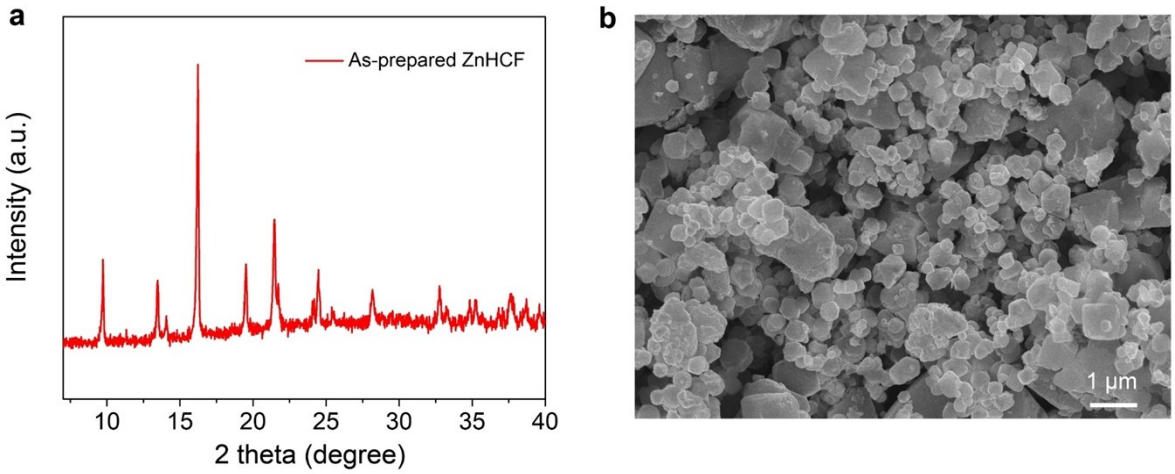

Fig. S25 (a) XRD pattern and (b) SEM image of the as-prepared ZnHCF. The XRD pattern of the as-prepared ZnHCF can be well-indexed to the rhombohedral structured $Zn_3[Fe(CN)_6]_2$.[23] The as-prepared ZnHCF displays particulate morphology with a size distribution ranging from 200 nm to several μm.

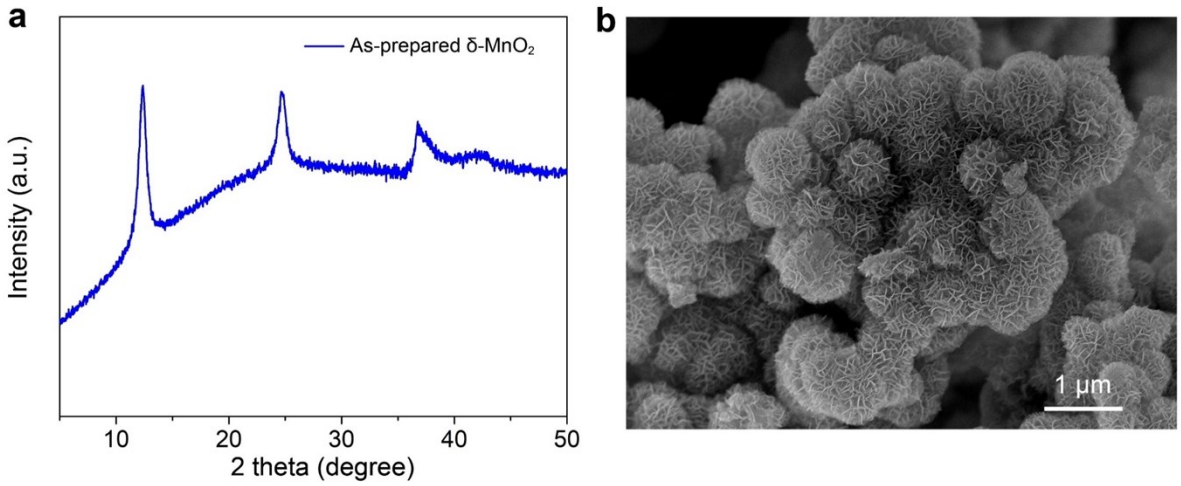

Fig. S26 (a) XRD pattern and (b) SEM image of the as-prepared MnO_2. The XRD pattern of the as-prepared MnO_2 is readily assigned to the typical signal of birnessite-type δ-MnO_2,[1] and the SEM image reveals that MnO_2 sample exhibits nanospheres morphology composed of uniform interconnected nanoflakes.

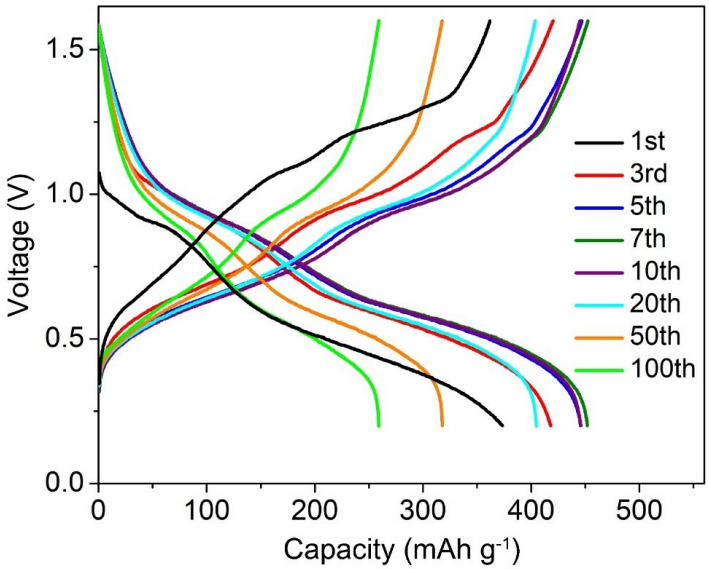

Fig. S27 Typical discharge/charge curves of Zn/V_2O_5 battery in 2 m W electrolyte at 0.2 A g^{-1}.

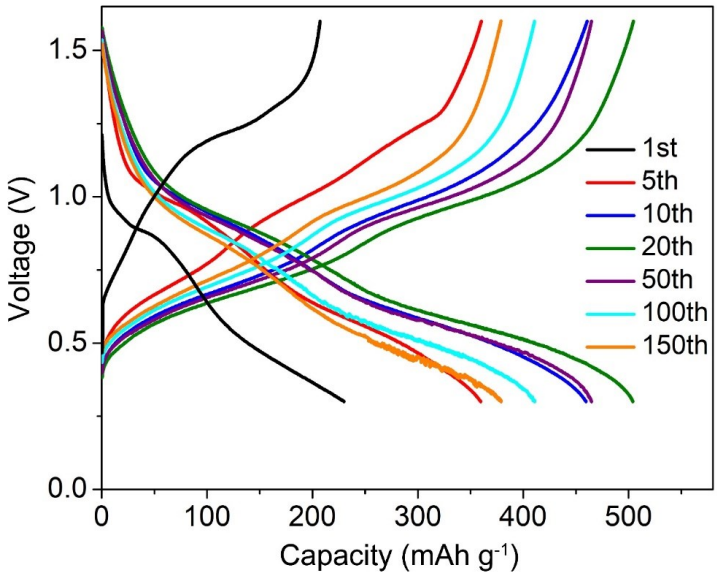

Fig. S28 Typical discharge/charge curves of Zn/V_2O_5 battery in W8D1 electrolyte at 0.2 A g^{-1}.

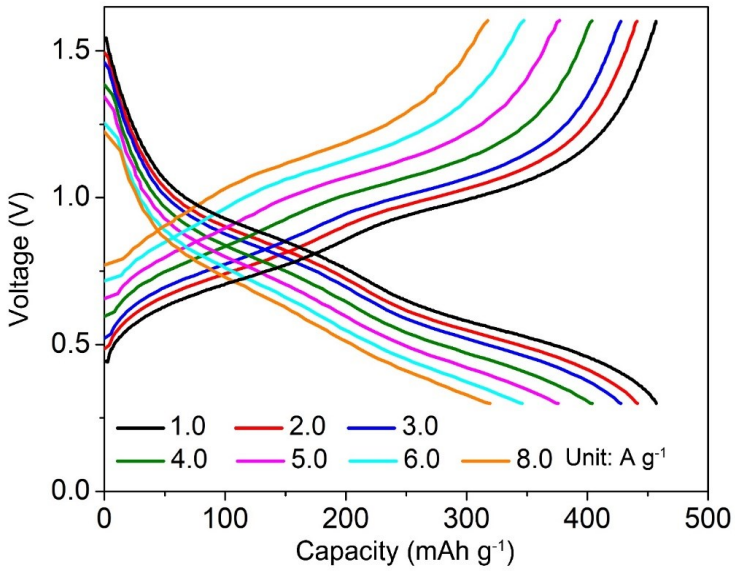

Fig. S29 Typical discharge/charge curves of Zn/V_2O_5 battery in W4D1 electrolyte at different current densities.

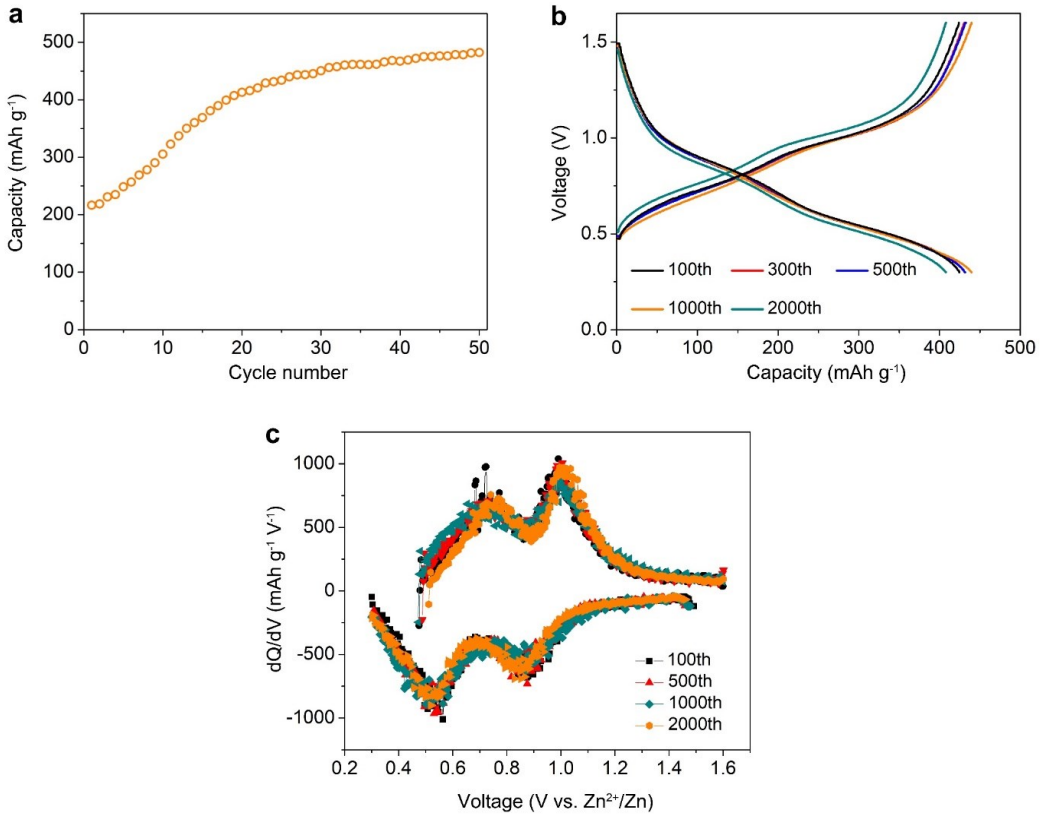

Fig. S30 (a) The initial 50 cycles of Zn/V_2O_5 battery in W4D1 electrolyte at 0.5 A g^{-1}. (b) Selected discharge/charge curves and (c) corresponding dQ/dV profiles at 2.0 A g^{-1}.

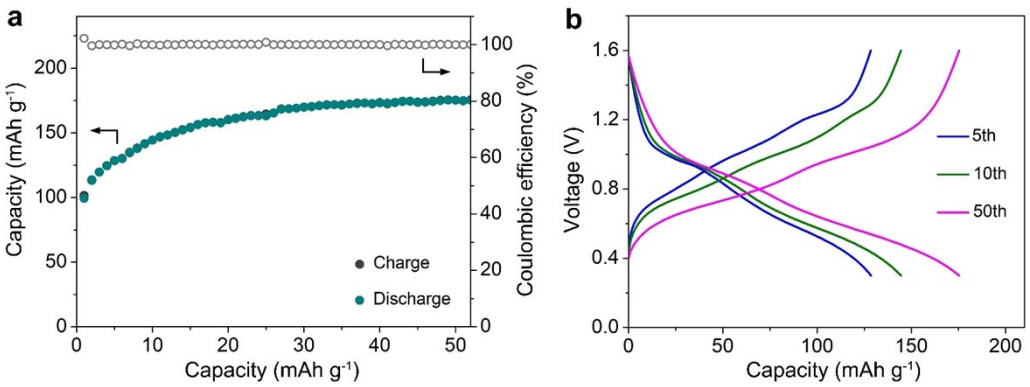

Fig. S31 (a) Cycling performance and (b) typical discharge/charge profiles of Zn/W4D1/V_2O_5 cell with a high-mass-loading V_2O_5 cathode (~11 mg cm^{-2}) and a thin Zn foil anode (20 μm thickness, ~14.28 mg cm^{-2} (11.7 mAh cm^{-2})). The test current is 2.2 mA cm^{-2} (200 mA g^{-1} for V_2O_5 cathode). After 50 cycles, this cell exhibits a reversible capacity of 175 mAh g^{-1} based on the total mass of cathode and anode. The utilization of Zn is around 4.42 mAh cm^{-2} and the DOD of Zn anode is calculated to be 37.7% (4.42÷11.7=37.7%).

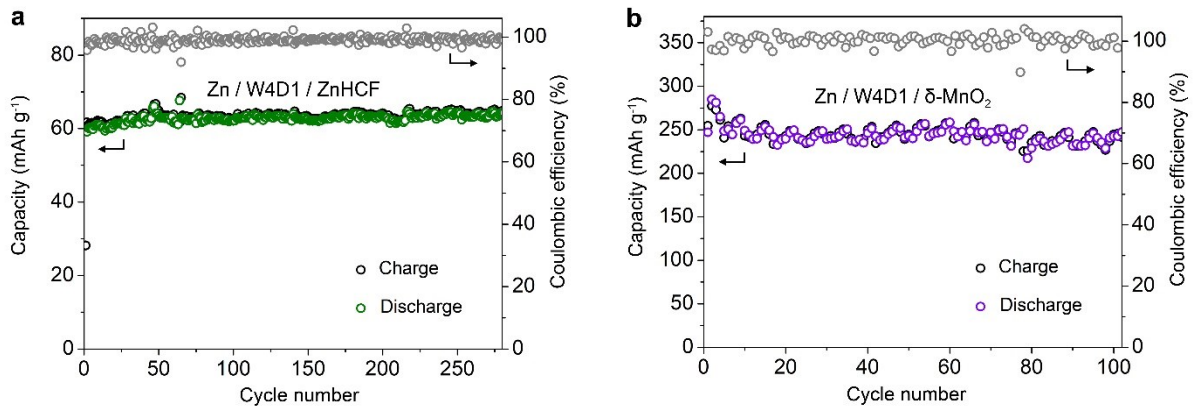

Fig. S32 Cycling stability of (a) Zn/W4D1/ZnHCF battery at 50 mA g^{-1} and (b) Zn/W4D1/δ-MnO_2 battery at 100 mA g^{-1}.

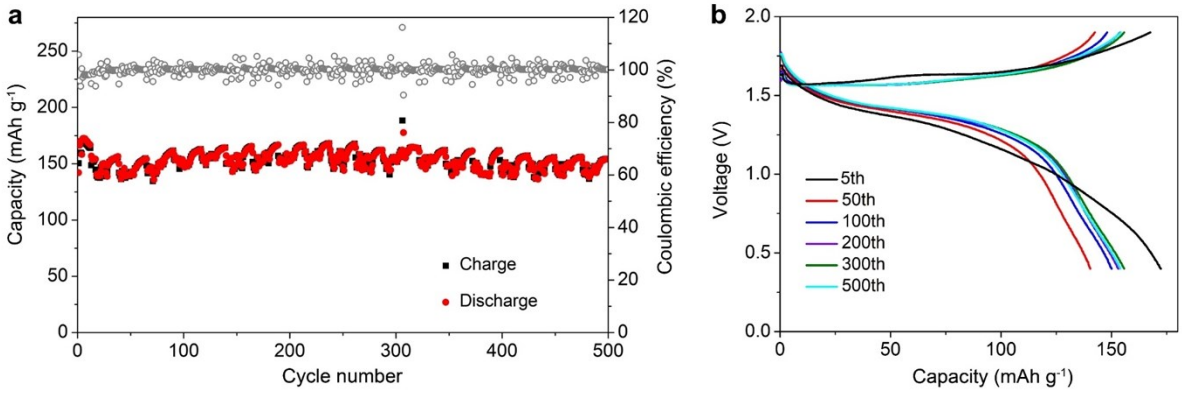

Fig. S33 (a) Cycling performance and (b) the selected charge/discharge curves of Zn/δ-MnO_2 battery in W4D1 electrolyte at 500 mA g^{-1}. The δ-MnO_2 electrode shows a reversible capacity of 154 mAh g^{-1} with a retention of 89.5% (compared to the highest discharge capacity of 172 mAh g^{-1} at the 5th cycle) after 500 cycles.

Table S1. Composition of electrolyte samples.

System	$Zn(OTf)_2$ salt	Water solvent	DMC solvent	Molar ratio (water:DMC)	Concentration (molality, mol kg^{-1})
2 m W	2 mmol	55.56 mmol	0	--	2 m
W8D1	2 mmol	34.17 mmol	4.27 mmol	8:1	2 m
W6D1	2 mmol	30.28 mmol	5.04 mmol	6:1	2 m
W4D1	2 mmol	24.67 mmol	6.17 mmol	4:1	2 m
W2D1	2 mmol	15.89 mmol	7.93 mmol	2:1	2 m

Table S2. Numbers of ions and solvent molecules (i.e., the composition) in the investigated simulation systems.

System	Zn^{2+}	OTf^-	DMC	Water
DMC-water			154	617
2 m W	50	100		1389
W8D1	50	100	107	854
W6D1	50	100	126	757
W4D1	50	100	154	617
W2D1	50	100	198	397

Table S3. Fitting results of the DMC Raman signal.

Electrolyte	Free DMC	DMC-Zn^{2+}
DMC	100%	--
W8D1	23.88%	76.12%
W6D1	26.68%	73.14%
W4D1	30.08%	69.92%
W2D1	34.61%	65.39%

It is worth noting that the content of DMC additive is changing in the H_2O+DMC electrolyte systems. Thus, the contents of DMC bound to Zn^{2+} in electrolyte samples (Table S1) are gradually increasing with the addition of DMC (from W8D1 to W2D1).

Table S4. Fitting results of the OTf^- Raman signal.

Electrolyte	FA	SSIP	CIP
2 m W	10.78%	68.92%	20.30%
W8D1	8.66%	44.19%	47.15%
W6D1	8.21%	38.27%	53.52%
W4D1	6.33%	33.62%	60.05%
W2D1	6.58%	25.68%	67.73%

Table S5. Comparison of CE and cycling life of this work with recently reported asymmetric Zn-based cells.

Electrode	Electrolyte	Average CE	Current density and plating capacity	Cycle number	Ref.
Zn foil (50 μm)	W4D1	99.8%	5 mA cm^{-2}; 2.5 mAh cm^{-2}	600	This work
Zn foil (50 μm)	2 M $ZnSO_4/H_2O$ + 40vol.% EG	98%	2 mA cm^{-2}; 1 mAh cm^{-2}	120	24
Zn foil (250 μm)	0.5 M $Zn(OTf)_2$/TEP-H_2O (7:3 by vol.)	93.71%	0.5 mA cm^{-2}; 0.5 mAh cm^{-2}	100	25
Zn foil (20 μm)	$Zn(TFSI)_2$/acetamide (molar ratio 1:7)	~98%	0.5 mA cm^{-2}; 0.5 mAh cm^{-2}	50	21
PVB@Zn foil (10 μm)	1 M $ZnSO_4/H_2O$	99.4%	4 mA cm^{-2}; 2 mAh cm^{-2}	100	17
Zn@ZnO-3D (100 μm)	2 M $ZnSO_4$ + 0.1 M $MnSO_4/H_2O$	99.55%	2 mA cm^{-2}; 0.5 mAh cm^{-2}	300	26
MOF-coated Zn foil (25 μm)	1 M $Zn(TFSI)_2/H_2O$	~99%	1 mA cm^{-2}; 0.5 mAh cm^{-2}	350	27
Zn foil (--)	DOL/$Zn(BF_4)_2$-based solid polymer electrolyte	99.34%	0.5 mA cm^{-2}; 0.5 mAh cm^{-2}	800	28
Zn foil (--)	$Zn(BF_4)_2$/[EMIM]BF_4-based ionic liquid electrolyte	99.36%	0.5 mA cm^{-2}; 0.5 mAh cm^{-2}	600	29
Zn foil (50 μm)	2 M $ZnSO_4/H_2O$ with addition of 50 v/v% MeOH (Anti-M-50%)	99.7%	1 mA cm^{-2}; 0.5 mAh cm^{-2}	900	16
Zn foil (--)	1.3 m $ZnCl_2/H_2O$-DMSO (4.3:1 by vol.)	99.5%	1 mA cm^{-2}; 0.5 mAh cm^{-2}	400	30

Table S6. Comparison of typical parameters and cycling performance of this work with recently reported symmetric Zn/Zn cells.

Electrode	Electrolyte	Areal capacity	Current density	Cycling life	DOD	Ref.
Zn foil (50 μm)	W4D1	2.5 mAh cm^{-2}	5 mA cm^{-2}	800 h	8.56%	This work
Zn foil (50 μm)	3 M $ZnSO_4/H_2O$ + 68vol.%EG	0.5 mAh cm^{-2}	5 mA cm^{-2}	160 h	1.71%	31
Zn foil (250 μm)	0.5 M $Zn(OTf)_2$/TEP	1.0 mAh cm^{-2}	1.0 mA cm^{-2}	220 h	0.68%	25
Zn foil (100 μm)	1 m $Zn(TFSI)_2$ + 20 m LiTFSI/H_2O	0.068 mAh cm^{-2}	0.2 mA cm^{-2}	170 h	~0.12%	32
Zn foil (~20 μm)	LZ-DES/2H_2O (LiTFSI:$Zn(TFSI)_2$: Urea:H_2O = 1:0.05:3.8:2 by molar)	0.2 mAh cm^{-2}	0.02 mA cm^{-2}	450 h	~1.8%	33
(002) Zn paper (50 μm)	2 M $Zn(OTf)_2/H_2O$	1.66 mAh cm^{-2}	10 mA cm^{-2}	200 h	5.69%	34
ZF@F-TiO_2 (Zn 30 μm)	1 M $ZnSO_4/H_2O$	1 mAh cm^{-2}	1 mA cm^{-2}	460 h	5.69%	35
Zn@ZIF-7 (20 μm)	2 M $ZnSO_4/H_2O$	0.5 mAh cm^{-2}	0.5 mA cm^{-2}	3000 h	4.27%	36
MXene-coated Zn (50 μm)	2 M $ZnSO_4/H_2O$	1 mAh cm^{-2}	0.5 mA cm^{-2}	350 h	3.42%	37
Zn@ZnO (100 μm)	2 M $ZnSO_4$ + 0.1 M $MnSO_4/H_2O$	1.25 mAh cm^{-2}	5 mA cm^{-2}	500 h	2.14%	26
Zn@HsGDY (--)	2 M $ZnSO_4/H_2O$	0.1 mAh cm^{-2}	2 mA cm^{-2}	2400 h	--	38

Supplementary References

[1] T. Sun, Q. Nian, S. Zheng, J. Shi and Z. Tao, *Small*, 2020, **16**, 2000597.

[2] L. Ma, M. A. Schroeder, O. Borodin, T. P. Pollard, M. S. Ding, C. Wang and K. Xu, *Nat. Energy*, 2020, **5**, 743–749.

[3] H. J. C. Berendsen, J. P. M. Postma, W. F. van Gunsteren, A. DiNola and J. R. Haak, *J. Chem. Phys.*, 1984, **81**, 3684–3690.

[4] W. D. Cornell, P. Cieplak, C. I. Bayly, I. R. Gould, K. M. Merz, D. M. Ferguson, D. C. Spellmeyer, T. Fox, J. W. Caldwell and P. A. Kollman, *J. Am. Chem. Soc.*, 1995, **117**, 5179–5197.

[5] T. Darden, D. York and L. Pedersen, *J. Chem. Phys.*, 1993, **98**, 10089–10092.

[6] J.-P. Hansen and I. R. McDonald, Theory of simple liquids, *Elsevier*, **2013**.

[7] W. Humphrey, A. Dalke and K. Schulten, *J. Mol. Graph.*, 1996, **14**, 33–38.

[8] C. J. Margulis, H. A. Stern and B. J. Berne, *J. Phys. Chem. B*, 2002, **106**, 12017–12021.

[9] H. Matsuyama and K. Motoyoshi, *Chem. Phys. Lett.*, 2021, **763**, 138246.

[10] M. Levesque, V. Sarou-Kanian, M. Salanne, M. Gobet, H. Groult, C. Bessada, P. A. Madden and A.-L. Rollet, *J. Chem. Phys.*, 2013, **138**, 184503.

[11] Frisch, M. J., et al. Gaussian 16, Revision A. 03. Gaussian, Inc., Wallingford, CT, **2016**.

[12] A. V. Marenich, C. J. Cramer and D. G. Truhlar, *J. Phys. Chem. B*, 2009, **113**, 6378–6396.

[13] J.-B. Brubach, A. Mermet, A. Filabozzi, A. Gerschel, D. Lairez, M. P. Krafft and P. Roy, *J. Phys. Chem. B*, 2001, **105**, 430–435.

[14] X. Bogle, R. Vazquez, S. Greenbaum, A. v. W. Cresce and K. Xu, *J. Phys. Chem. Lett.*, 2013, **4**, 1664–1668.

[15] X. Chen, X. Shen, T.-Z. Hou, R. Zhang, H.-J. Peng and Q. Zhang, *Chem*, 2020, **6**, 2242–2256.

[16] J. Hao, L. Yuan, C. Ye, D. Chao, K. Davey, Z. Guo and S. Qiao, *Angew. Chem. Int. Ed.*, 2021, **60**, 7366–7375.

[17] J. Hao, X. Li, S. Zhang, F. Yang, X. Zeng, S. Zhang, G. Bo, C. Wang and Z. Guo, *Adv. Funct. Mater.*, 2020, **30**, 2001263.

[18] L. Suo, O. Borodin, T. Gao, M Olguin, J. Ho, X. Fan, C. Luo, C. Wang and K. Xu, *Science*, 2015, **350**, 6263.

[19] J. Zhang, Z. Cao, L. Zhou, G. Park, L. Cavallo, L. Wang, H. N. Alshareef, Y. K. Sun and J. Ming, *ACS Energy Lett.* 2020, **5**, 3124–3131.

[20] K. Xu, Y. Lam, S. S. Zhang, T. R. Jow and T. B. Curtis, *J. Phys. Chem. C*, 2007, **111**, 7411–7421.

[21] H. Qiu, X. Du, J. Zhao, Y. Wang, J. Ju, Z. Chen, Z. Hu, D. Yan, X. Zhou and G. Cui, *Nat. Commun.*, 2019, **10**, 5374.

[22] F. Wang, O. Borodin, M. S. Ding, M. Gobet, J. Vatamanu, X. Fan, T. Gao, N. Eidson, Y. Liang, W. Sun, S. Greenbaum, K. Xu and C. Wang, *Joule*, 2018, **2**, 927–937.

[23] L. Zhang, L. Chen, X. Zhou and Z. Liu, *Adv. Energy Mater.*, 2015, **5**, 1400930.

[24] N. Chang, T. Li, R. Li, S. Wang, Y. Yin, H. Zhang and X. Li, *Energy Environ. Sci.*, 2020, **13**, 3527–3535.

[25] A. Naveed, H. Yang, J. Yang, Y. Nuli and J. Wang, *Angew. Chem. Int. Ed.*, 2019, **58**, 2760–2764.

[26] X. Xie, S. Liang, J. Gao, S. Guo, J. Guo, C. Wang, G. Xu, X. Wu, G. Chen and J. Zhou, *Energy Environ. Sci.*, 2020, **13**, 503–510.

[27] L. Cao, D. Li, T. Deng, Q. Li and C. Wang, *Angew. Chem. Int. Ed.*, 2020, **59**, 19292–19296.

[28] L. Ma, S. Chen, X. Li, A. Chen, B. Dong and C. Zhi, *Angew. Chem. Int. Ed.*, 2020, **59**, 23836–23844.

[29] L. Ma, S. Chen, N. Li, Z. Liu, Z. Tang, J. A. Zapien, S. Chen, J. Fan and C. Zhi, *Adv. Mater.*, 2020, **32**, 1908121.

[30] L. Cao, D. Li, E. Hu, J. Xu, T. Deng, L. Ma, Y. Wang, X.-Q. Yang and C. Wang, *J. Am. Chem. Soc.*, 2020, **142**, 21404–21409.

[31] R. Qin, Y. Wang, M. Zhang, Y. Wang, S. Ding, A. Song, H. Yi, L. Yang, Y. Song, Y. Cui, J. Liu, Z. Wang, S. Li, Q. Zhao and F. Pan, *Nano Energy*, 2021, **80**, 105478.

[32] F. Wang, O. Borodin, T. Gao, X. Fan, W. Sun, F. Han, A. Faraone, J. A. Dura, K. Xu and C. Wang, *Nat. Mater.*, 2018, **17**, 543–549.

[33] J. Zhao, J. Zhang, W. Yang, B. Chen, Z. Zhao, H. Qiu, S. Dong, X. Zhou, G. Cui and L. Chen, *Nano Energy*, 2019, **57**, 625–634.

[34] D. Yuan, J. Zhao, H. Ren, Y. Chen, R. Chua, E. T. J. Jie, Y. Cai, E. Edison, W. J. Manalastas, M. W. Wong and M. Srinivasan, *Angew. Chem. Int. Ed.*, 2021, **60**, 7213–7219.

[35] Q. Zhang, J. Luan, X. Huang, Q. Wang, D. Sun, Y. Tang, X. Ji and H. Wang, *Nat. Commun.*, 2020, **11**, 3961.

[36] H. Yang, Z. Chang, Y. Qiao, H. Deng, X. Mu, P. He and H. Zhou, *Angew. Chem. Int. Ed.*, 2020, **59**, 9377–9381.

[37] N. Zhang, S. Huang, Z. Yuan, J. Zhu, Z. Zhao and Z. Niu, *Angew. Chem. Int. Ed.*, 2021, **60**, 2861–2865.

[38] Q. Yang, Y. Guo, B. Yan, C. Wang, Z. Liu, Z. Huang, Y. Wang, Y. Li, H. Li, L. Song, J. Fan and C. Zhi, *Adv. Mater.*, 2020, **32**, 2001755.